Preprint version of:
Suarez, A., Heredia, G., & Ollero, A. (2018). Physical-virtual impedance control in ultralightweight and compliant dual-arm aerial manipulators. IEEE Robotics and Automation Letters, 3(3), 2553-2560.

Physical-Virtual Impedance Control in Ultra-Lightweight and Compliant Dual Arm Aerial Manipulators

Alejandro Suarez, Guillermo Heredia, and Anibal Ollero

***Abstract*— Dual arm aerial manipulation requires the design and development of high performance robotic arms in terms of safety, robustness, and force/torque/impedance control, taking into account the integration in the aerial platform, the strong weight constraints, and the technological limitations of the servo actuators. A compliant joint arm also improves the response of the aerial manipulator to collisions and external forces during the flight operation. This paper evaluates the control capabilities in a lightweight manipulator built with smart servo actuators and a spring-lever transmission mechanism which provides joint compliance and deflection measurement. The dynamic model of a compliant joint is validated through frequency identification, demonstrating how virtual variable impedance can be achieved without a second motor. Mechanical joint compliance is the base of the Cartesian impedance control scheme of the dual arm system, integrated with the controller of the aerial platform. A stereo vision system provides the Cartesian deflection of the end effector, derived from the definition of an equivalent stiff joint manipulator, allowing the estimation and control of the contact forces. Experimental results validate the developed concepts.**

I. INTRODUCTION

It is expected that in a near future aerial manipulators can replace human workers in the realization of certain inspection and maintenance operations, where the high risk and required time in the deployment of resources to difficult access areas involve a significant cost for many companies. Installation of sensors in polluted zones, insulation of leaks in high altitude pipes, or the visual inspection and repair of wind turbines are some illustrative application examples. Although nowadays it is possible to find a wide variety of commercially available aerial platforms, the development of very low weight, low cost and high performance robotic arms to be integrated in a multi-rotor vehicle is still a technological challenge. Several research prototypes have been proposed and tested in indoors [1][2] and outdoors [3][4], including dual arm manipulators [5][6]. Most robotic arms intended for aerial manipulation are built with smart servo actuators (Herkulex or Dynamixel) due to their low cost and weight, ease of assembly and integration. However, their limitations in terms of feedback and control cannot be ignored. The embedded microcontroller and the serial communication bus reduce in practice the update rate to 50 – 100 Hz, far away from the 1 KHz provided by industrial manipulators. Servo actuators only accept as input the position reference and the desired motion time (playtime), and there is no direct feedback or control over the motor torque or speed.

The benefits of mechanical compliance in terms of safety and robustness are evident in many aerial manipulation tasks involving contact forces with the environment [7]-[9]. Several high performance compliant joint mechanisms [10][11] and variable stiffness actuators [12][13] have been developed for ground robotics. Now the current challenge is the mechatronic design and development of very low weight and compliant manipulators that can be integrated in multirotor platforms, taking into account the strong limitations in terms of payload, dynamic coupling and influence to external forces [14][15]. The control of fixed-base manipulator arms with elastic joints has been treated in the literature for the last 30 years [16][17]. Impedance control has been used frequently for controlling these compliant manipulators [18][17]. Impedance control has also been implemented in aerial manipulators with a rigid-link arm [19][20].

In our previous work we developed and demonstrated the capabilities of three prototypes of lightweight and compliant joint robotic arms. A pair of extension springs connecting the stroke of a linear servo with the forearm are introduced in [22] for estimating the mass of grasped objects and for detecting collisions against obstacles based on the deflection of the elbow joint. The 3-DOF robotic arm described in [23] makes use of a spring-lever mechanism installed between the servo shaft and the output link for transmitting and estimating the torque in the joint, demonstrating contact force control and obstacle localization. Finally, an anthropomorphic compliant and lightweight dual arm aerial manipulator is presented in [24], showing bimanual object grasping in outdoor flights.

This paper explores the force and virtual impedance control capabilities in an anthropomorphic, compliant and lightweight (1.3 kg) dual arm system integrated in a hexarotor platform. The dynamic model of the compliant actuator is analyzed in the first place, describing later the design of the controller for achieving virtual variable impedance to external load. The concept of Cartesian deflection is then defined and applied to bimanual force-position control, introducing in this work a stereo vision system for estimating the deviation of the markers attached to the left/right arms with respect to their position in an equivalent stiff joint dual arm manipulator. The developed models are validated experimentally, evaluating the performance of the virtual variable impedance controller in a single joint, and the impedance controller of the dual arm manipulator in hovering conditions.

The rest of the paper is organized as follows. Section II describes the dual arm aerial manipulator. Section III presents the model of the compliant actuator, the dual arm system, and the aerial manipulator. Section IV explains the control method for achieving virtual variable impedance in a compliant joint, the force/position controller in the dual arm, and the control scheme of the whole aerial manipulator. Section V presents the results, summarizing the conclusions in Section VI.

A. Suarez (asuarezfm@us.es), G. Heredia (guiller@us.es), and A. Ollero (aollero@us.es) are with the Robotics, Vision and Control Group at the University of Seville, Spain, http://grvc.us.es.

II. Compliant Joint, Dual Arm Aerial Manipulator

Bimanual manipulation extends the range of operations that an aerial robot is able to perform with respect to the single arm case, allowing for example the transportation, installation and retrieval of two sensor devices simultaneously, grasping large objects, operating on flight with one arm while the other is grabbed to a fixed point, or tele-operating one arm using the second arm in eye-in-hand camera configuration. Mechanical joint compliance is a highly desirable feature for an aerial manipulator, as it prevents that the contact forces are rigidly propagated to the aerial vehicle, protects the actuators against impacts and overloads, and it also allows the estimation and control of endogenous and exogenous wrenches in terms of deflection [23], contributing to increase safety and reliability.

The anthropomorphic, compliant and lightweight dual arm system depicted in Figure 1 was developed from the scratch at the Robotics, Vision and Control Group of the University of Seville. Each arm provides four degrees of freedom (DOF) for end effector positioning in a kinematic configuration similar to the human arm [24]: flexion/extension (pitch), abduction/ adduction (roll), medial/lateral rotation (yaw) of the shoulder, flexion-extension (pitch) of the elbow. Its main features are:

- Very low weight (1.3 kg in total) and low inertia, so the influence of arms motion over the UAV is reduced.
- Mechanical joint compliance, integrating a spring-lever mechanism in all the joints of both left and right arms.
- High mechanical servo protection thanks to a carefully designed aluminum frame structure and flange bearings.

This work introduces as novelty a stereo vision system that allows the estimation and control of interaction forces in the arms in terms of the deflection measured at the end effector. A ZED camera installed over the shoulder structure is visually focused on two markers attached to the grippers, obtaining the position and velocity from an Extended Kalman Filter.

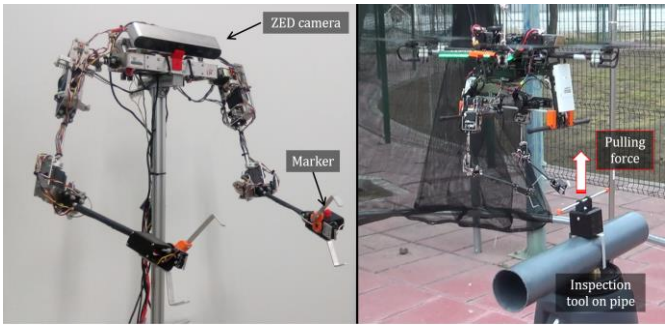

Figure 1. Anthropomorphic, compliant and lightweight dual arm manipulator (left) integrated in hexarotor platform during the bimanual tool grasping in outdoors (right). The stereo camera head is used for estimating the Cartesian deflection of the end effector due to external forces over the compliant joints.

The aerial platform is a hexarotor manufactured by Drone Tools, providing 2.5 kg payload and around 25 minutes flight time with no load. Besides the dual arm, it integrates an Intel NUC computer board for image processing and control, a 5.8 GHz wireless link, and an A2 industrial autopilot from DJI. The arms are disposed in such a way that the landing gear does not interfere in the workspace of the arms and the center of mass is aligned with the vertical axis.

III. Modeling

A. Compliant Actuator Dynamics

One of the main goals of this paper demonstrating the capabilities of a lightweight and compliant joint manipulator, which requires firstly a precise knowledge about this kind of actuators. Let us consider the compliant actuator depicted in Figure 2 along with its model, assimilated to a series elastic actuator consisting of a Herkulex DRS-0101 servo and the spring-lever transmission mechanism. The servo accepts as reference the desired goal position/trajectory θ_{ref}, generating internally a trapezoidal velocity profile which ensures that the servo reaches the reference at the specified playtime. The feedback provided by the device is its current position θ and differential position $\dot{\theta}$. A first order dynamics characterized by a time constant T_{servo}, and a delay T_{delay} associated to the serial communications are identified experimentally, so the servo can be modeled by the following transfer function:

$$G_{servo}(s) = \frac{\theta}{\theta_{ref}} = \frac{e^{-T_{delay} \cdot s}}{1 + T_{servo} \cdot s} \quad (1)$$

The compliant transmission mechanism is represented by a spring-damper system characterized by its physical stiffness k_p and damping d_p. The torque transmitted by the spring-lever mechanism will depend on the deflection angle, defined as the difference between the servo shaft angular position and the output link angular position:

$$\tau = k_p(\theta - q) + d_p(\dot{\theta} - \dot{q}) = k_p \Delta\theta + d_p \Delta\dot{\theta} \quad (2)$$

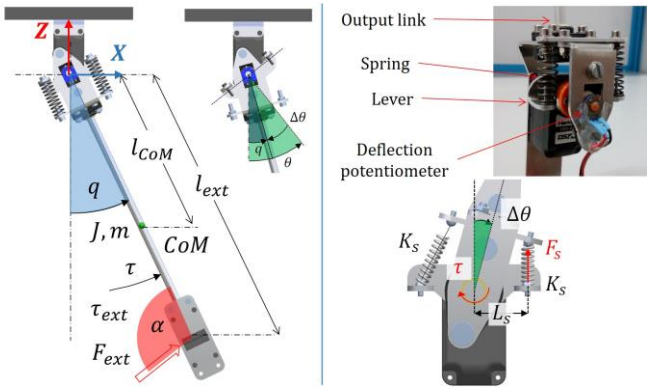

Figure 2. Model of the compliant joint actuator and mechanical construction.

The torque delivered by the servo motor, τ_m, is dedicated to compensate the friction of the gearbox, τ_f, and the rotor inertia b, transmitting the torque τ to the output link:

$$\tau_m = b\ddot{\theta} + \tau_f + \tau \quad (3)$$

The torque transmitted by the spring-lever and the external torque accelerate the output link and compensate the gravity:

$$\tau + \tau_{ext} = J\ddot{q} + mgl_{COM}sin(q) \quad (4)$$

Here m and J are the mass and inertia of the output link, respectively, g is the gravity constant, and l_{COM} is the distance from the servo shaft to the center of mass. The parameters of the compliant joint under study (Section V-A) are summarized in Table 1. The mass, inertia and distance to the CoM of the output link are obtained from the CAD model, whereas the parameters of the servo were identified experimentally.

Table 1. Parameters of the compliant joint actuator.

Servo Actuator		Spring-Lever		Output Link	
T_{servo}	0.035 s	k_p	1.2 Nm/rad	J	0.0044 kgm^2
T_{delay}	0.02 s	d_p	0.02 Nms/rad	m	0.118 kg
$\tau_{m,stall}$	1.17 Nm	$\Delta\theta_{max}$	30 deg	l_{CoM}	0.132 m

The natural stiffness of the compliant joint, k_p, is obtained from the stiffness of the compression springs, K_s (given by the manufacturer), and the lever length, L_s, taking into account that the force generated by the spring, ΔF_s, is approximately proportional [23] to the angular deflection, $\Delta\theta$, resulting that:

$$k_p = \frac{\Delta\tau}{\Delta\theta} = \frac{\Delta F_s \cdot L_s}{\Delta\theta} \cong \frac{(K_s \cdot L_s \cdot \Delta\theta) \cdot L_s}{\Delta\theta} = K_s \cdot L_s^2 \quad (5)$$

This was illustrated in Figure 2. The physical damping d_p was obtained experimentally from the Fast Fourier Transform of the deflection signal, exciting the servo with a sine chirp position reference (see Section V-A). The matching between the measured deflection and the simulation model given by Equations (1)–(5) determines the value of this parameter.

B. Anthropomorphic, Compliant Dual Arm

The reference frames, joint variables, lengths and position vectors used to describe the kinematics of the dual arm system are depicted in Figure 3. Superscript $i = \{1, 2\}$ denotes the left/right arm, and subscript $j = \{1,2,3,4\}$ indicates the joint in the following order: shoulder pitch (q_1^i), roll (q_2^i), yaw (q_3^i), and elbow pitch (q_4^i). Each arm defines a coordinate system $\{\boldsymbol{i}\} = \boldsymbol{X^i Y^i Z^i}$ whose origin is located at the intersection of the three joints of the shoulder. The servo shaft and output link angular position vectors are denoted as $\boldsymbol{\theta^i}$ and $\boldsymbol{q^i}$ respectively.

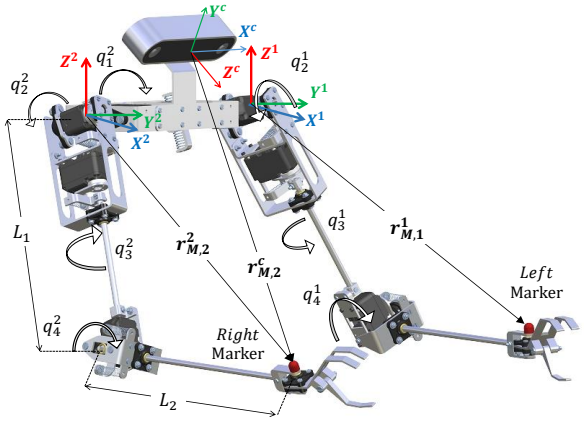

Figure 3. Kinematic model of the anthropomorphic dual arm with camera head. The cameras are focused on the color markers attached at the wrist.

Let us consider the markers attached to the wrist point of the arms. As seen in Figure 1 and in Figure 3, the camera head is visually focused on these markers whose Cartesian position referred to the camera frame, $\boldsymbol{r_{M,i}^c}$, is provided by the vision system. Since the rotation and translation of the camera w.r.t. each arm are known, then the position of the markers w.r.t. the arms frame, denoted as $\boldsymbol{r_{M,i}^i}$, is obtained. The Cartesian and joint positions associated to these points are related through the equations of the forward /inverse kinematic model [24]:

$$\boldsymbol{r_{M,i}^i = FK^i(q_{M,i}^i)} \;\; ; \;\; \boldsymbol{q_{M,i}^i = IK^i(r_{M,i}^i)} \quad (6)$$

This work assumes that the shoulder roll joint is redundant and its value is set to $q_2^i = \varphi_i \sim \pm 10\ deg$ for bimanual tasks like grasping. Since the solution to the shoulder pitch joint q_1^i is double (elbow up/down), which also affects to the shoulder yaw joint q_3^i, it was necessary to impose that the resulting join values ensured the elbow down configuration.

The Cartesian deflection of the manipulator referred to the markers is defined as the difference between the position of this point in an equivalent stiff-joint manipulator and its real position in the compliant manipulator:

$$\boldsymbol{\Delta l_{M,i}^i = FK^i\left(\theta_{M,i}^i\right) - FK^i\left(q_{M,i}^i\right) = FK^i\left(\theta_{M,i}^i\right) - r_{M,i}^i} \quad (7)$$

This definition is useful for expressing the dynamics of the end effector in the task space in the mass-spring-damper form:

$$\boldsymbol{M^i \Delta\ddot{l}^i + D_C^i \Delta\dot{l}^i + K_C^i\left(\Delta l^i - \Delta l_0^i\right) + \Delta l_G^i = F^i + F_{ext}^i} \quad (8)$$

Here $\boldsymbol{M^i = m_i I_3} \in \Re^{3\times3}$ is the mass matrix of the upper arm-forearm links of the i-th arm, $\boldsymbol{D_C^i}$ and $\boldsymbol{K_C^i} \in \Re^{3\times3}$ are the Cartesian damping and stiffness of the virtual compliant end effector, $\boldsymbol{\Delta l_0}$ is the deflection offset, and $\boldsymbol{\Delta l_G^i}$ is the deflection due to gravity. The model assumed in Equation (8) is derived from the observation of the Cartesian deflection when the end effector suffers an impact (impulsive response). Section V-C will show that the natural response of the compliant arms can be assimilated to a second order dynamics in the mentioned form for small deflections. The Cartesian stiffness matrix can be computed from the Jacobian and the joint stiffness matrix:

$$\left.\begin{aligned} \boldsymbol{F^i = K_C^i \Delta l^i = K_C^i J^i \Delta\theta^i} \\ \boldsymbol{F^i = (J^{i,T})^{-1} K_p^i \Delta\theta^i} \end{aligned}\right\} \rightarrow \boldsymbol{K_C^i = (J^{i,T})^{-1} K_p^i (J^i)^{-1}} \quad (9)$$

where $\boldsymbol{J^i}$ is the Jacobian of the i-th arm and $\boldsymbol{K_p^i = diag(k_j^i)}$ is the physical joint stiffness matrix. The Cartesian damping will in general depend on the joint position, as the friction in the flange bearings varies with the load supported by the shaft. An approximated value can be determined experimentally for a particular configuration of the arms in a similar way to the method described in Section III-A. If the mass and stiffness parameters are known, then the damping $\boldsymbol{D_C^i}$ is obtained from the matching between the measured and simulated response of the Cartesian deflection to an impulsive or sine chirp signal (see Section V-C). Alternatively, if the physical joint damping $\boldsymbol{D_p^i = diag\{d_j^i\}} \in \boldsymbol{\Re^{4\times4}}$ is known, then the Cartesian damping matrix can be derived in the same way as done in equation (9).

It is interesting to note that the joint deflection and torque can be also computed from the inverse kinematics as follows:

$$\boldsymbol{\Delta\theta_{M,i}^i = \theta_{M,i}^i - IK^i(r_{M,i}^i)} \;\; ; \;\; \boldsymbol{\tau^i = K_p^i \cdot \Delta\theta_{M,i}^i} \quad (10)$$

Here $\boldsymbol{\tau^i}$ is the torque of the i-th arm. The resolution of the inverse kinematics in (10) imposes that $q_2^i = \varphi_i$ is known.

C. Aerial Manipulator Kinematics and Dynamics

In the definition of an aerial manipulation application, it is convenient to consider four coordinate systems related to the perception, navigation and manipulation tasks, as depicted in Figure 4: the Earth fixed frame $\{\boldsymbol{E}\}$, the multirotor base frame $\{\boldsymbol{B}\}$, the manipulator frame $\{\boldsymbol{i}\}$, and the task/workspace frame $\{\boldsymbol{T}\}$. A certain point $\boldsymbol{p}$ within the workspace can be expressed

in the manipulator's or in the Earth frame simply multiplying by the corresponding transformation matrices:

$$\begin{bmatrix} \boldsymbol{p^i} \\ 1 \end{bmatrix} = \boldsymbol{T_T^i} \cdot \begin{bmatrix} \boldsymbol{p} \\ 1 \end{bmatrix} \;\; ; \;\; \begin{bmatrix} \boldsymbol{p^E} \\ 1 \end{bmatrix} = \boldsymbol{T_T^E} \cdot \begin{bmatrix} \boldsymbol{p} \\ 1 \end{bmatrix} = \boldsymbol{T_B^E T_i^B T_T^i} \cdot \begin{bmatrix} \boldsymbol{p} \\ 1 \end{bmatrix} \quad (11)$$

Here $\boldsymbol{T_T^i}$, $\boldsymbol{T_B^E}$, $\boldsymbol{T_i^B}$ and are homogeneous matrices.

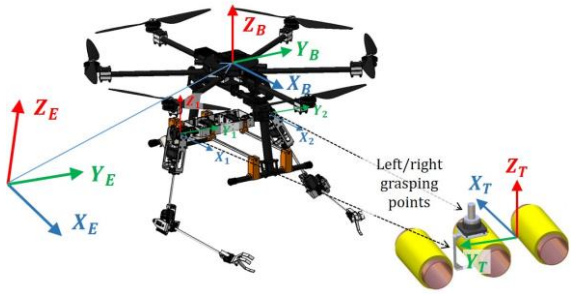

Figure 4. Coordinate systems of the dual arm aerial manipulator in a tool retrieval task. Earth, base, manipulator and task (workspace) frames.

The dynamic model of a compliant joint, dual arm aerial manipulator can be derived from the Newton-Euler method based on the interpretation of the energy of the system:

$$\frac{d}{dt}\left\{\frac{\partial L}{\partial \dot{\boldsymbol{\xi}}}\right\} - \frac{\partial L}{\partial \boldsymbol{\xi}} = \boldsymbol{\Gamma} \;\; ; \;\; L = K - V \quad (12)$$

Here L is the Lagrangian, K is the kinetic energy and V is the potential energy. The vector of generalized coordinates $\boldsymbol{\xi}$ includes the position of the center of mass of the aerial robot, $\boldsymbol{r_{CoM}} \in \Re^3$, its attitude, $\boldsymbol{\eta} \in \Re^3$, and the servo and output link angular positions, $\boldsymbol{\theta^i}$ and $\boldsymbol{q^i} \in \Re^4$:

$$\boldsymbol{\xi} = \left[\boldsymbol{r_{CoM}^T}, \boldsymbol{\eta^T}, \boldsymbol{\theta^{1,T}}, \boldsymbol{q^{1,T}}, \boldsymbol{\theta^{2,T}}, \boldsymbol{q^{2,T}}\right]^T \in \Re^{22} \quad (13)$$

The generalized force vector $\boldsymbol{\Gamma}$ represents the forces and moments generated by the propellers, the torque of the servo motors, and the external forces acting over the arms links:

$$\boldsymbol{\Gamma} = \left[\boldsymbol{F_{XYZ}^T}, \boldsymbol{\tau_{\varphi\theta\psi}^T}, \boldsymbol{\tau_m^{1,T}}, \boldsymbol{\tau_{ext}^{1,T}}, \boldsymbol{\tau_m^{2,T}}, \boldsymbol{\tau_{ext}^{2,T}}\right]^T \in \Re^{22} \quad (14)$$

The kinetic energy of the aerial manipulator is the sum of the contributions of the platform and each link of the arms:

$$T = \frac{1}{2}\begin{pmatrix} \dot{\boldsymbol{r}}_{\boldsymbol{CoM}} \\ \dot{\boldsymbol{\eta}} \end{pmatrix}^T \begin{bmatrix} m_T \cdot \boldsymbol{I_{3\times3}} & \boldsymbol{0} \\ \boldsymbol{0} & \boldsymbol{J_T} \end{bmatrix} \begin{pmatrix} \dot{\boldsymbol{r}}_{\boldsymbol{CoM}} \\ \dot{\boldsymbol{\eta}} \end{pmatrix} + \frac{1}{2}\sum_{i=1}^{2}\sum_{j=1}^{4} \begin{pmatrix} \dot{\boldsymbol{r}}_{\boldsymbol{j}}^{\boldsymbol{i}} \\ \boldsymbol{\omega}_{\boldsymbol{j}}^{\boldsymbol{i}} \end{pmatrix}^T \begin{bmatrix} m_j^i \cdot \boldsymbol{I_{3\times3}} & \boldsymbol{0} \\ \boldsymbol{0} & \boldsymbol{J_j^i} \end{bmatrix} \begin{pmatrix} \dot{\boldsymbol{r}}_{\boldsymbol{j}}^{\boldsymbol{i}} \\ \boldsymbol{\omega}_{\boldsymbol{j}}^{\boldsymbol{i}} \end{pmatrix} \quad (15)$$

where m_T and $\boldsymbol{J_T}$ are the total mass and inertia of the robot, m_j^i and $\boldsymbol{J_j^i}$ are the mass and inertia of the j-th link of the i-th arm, whose translational and angular speed are represented as $\dot{\boldsymbol{r}}_{\boldsymbol{j}}^{\boldsymbol{i}}$ and $\boldsymbol{\omega}_{\boldsymbol{j}}^{\boldsymbol{i}}$. The potential energy comprises the gravity term and the elastic potential energy stored in the compliant joints:

$$V = m_T g \boldsymbol{r_{CoM}} \begin{pmatrix} 0 \\ 0 \\ 1 \end{pmatrix} + \frac{1}{2}\sum_{i=1}^{2} (\boldsymbol{\theta^i} - \boldsymbol{q^i})^T \boldsymbol{K^i} (\boldsymbol{\theta^i} - \boldsymbol{q^i}) \quad (16)$$

where g is the gravity constant, and $\boldsymbol{K^i} = diag\left(k_j^i\right)$ is the stiffness diagonal matrix of the i-th arm. The dynamic model can be expressed in the usual matrix form:

$$\boldsymbol{M}(\boldsymbol{\xi})\ddot{\boldsymbol{\xi}} + \boldsymbol{C}\left(\boldsymbol{\xi}, \dot{\boldsymbol{\xi}}\right) + \boldsymbol{G}(\boldsymbol{\xi}) + \boldsymbol{K}(\boldsymbol{\xi}) + \boldsymbol{D}(\boldsymbol{\xi}) = \boldsymbol{\Gamma} \quad (17)$$

Here $\boldsymbol{M}$ is the generalized inertia matrix, $\boldsymbol{C}$ represents the centrifugal and Coriolis forces, whereas $\boldsymbol{G}$, $\boldsymbol{K}$ and $\boldsymbol{D}$ represent the gravity, elastic and damping components, respectively. The square inertia matrix $\boldsymbol{M} \in \Re^{22\times22}$ can be partitioned in submatrices representing the dynamic coupling between the multirotor and the arms. In this way, the submatrices $\boldsymbol{M_{rq1}}$ and $\boldsymbol{M_{\eta q1}}$ represent the inertia coupling terms between the translational and rotational dynamics of the multirotor and the first arm, and $\boldsymbol{M_{q1q2}}$ include the coupling terms representing how the movement of one arm affects the dynamics of the other arm. Vector $\boldsymbol{C}$ can also be decomposed in subvectors for each group of generalized coordinates. Thus, $\boldsymbol{C_{q1}}$ corresponds to the Coriolis and centrifugal terms of the dynamics of the first arm, which include coupling terms with the dynamics of the aerial platform and the other arm. This will be used in next section to compensate the coupling terms in the controllers.

IV. CONTROL

A. Control Structure of the Aerial Manipulator

This section briefly presents the proposed control system for the whole dual arm aerial manipulator, depicted in Figure 5. The aerial manipulator consists of the multirotor platform and the dual arm manipulator, whose input is the position reference of the servos, and its output are the servo position, the joint deflection and their time derivatives. A model based force-torque estimator integrates this information, used by the arms controller and the multirotor controller. The multirotor state estimation is also used by the arms and the multirotor controllers. The task manager implements the functionalities of the robot, like navigation, grasping, tool installation and retrieve, etc. This functional block generates the position or trajectory references for the aerial manipulator using the information given by the perception and navigation systems, following the sequence of operations indicated by the mission planner.

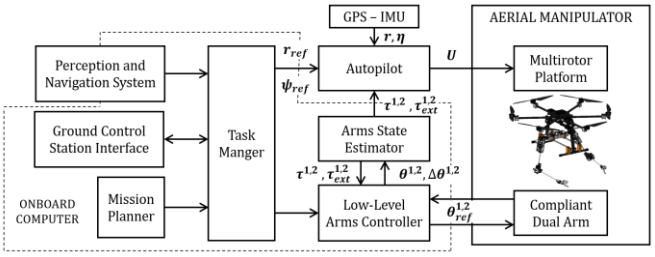

Figure 5. Dual arm aerial manipulator control architecture.

The multirotor controller is responsible of stabilizing the attitude and global position of the aerial vehicle, taking into account and compensating the movements of the arms and the interaction wrenches with the environment. The aerial manipulator implements a multirotor controller based on integral backstepping which follows the developments in [25] and [6], adapted to the dynamic model of the dual arm aerial manipulator in Equation (17). The impedance controller used for both arms is described in the following subsection for a single joint case, and the Cartesian impedance controller for the arms in the next subsection.

B. Virtual Variable Impedance in Compliant Joint

According to the model introduced in Section III-A, the compliant joint is characterized by its inertia J, damping d_p

and stiffness k_p, which depend on the physical realization of the joint. These parameters may have a significant influence in the behavior of the aerial manipulator when impact and contact forces arise during the realization of certain operations executed on flight. Then, it would result convenient to vary the apparent stiffness, damping or inertia of the joints depending on the particular task, but without increasing the weight of the actuator, so no additional mass should be added. This work proposes the implementation of a virtual variable impedance behavior at joint level based on the feedback and control of the joint deflection. The superscript is omitted for clarity since the same controller is used for both arms.

Let q_d be the desired link trajectory for an arbitrary link. Then, the desired motor positions can be obtained from q_d with gravity compensation:

$$\theta_d = q_d + k_p^{-1} g(q_d) \tag{18}$$

Here k_p is the physical stiffness. The equations governing the dynamics of the output link can be obtained extracting the corresponding rows in Eq. (17). The damping coefficient of the elastic joint is usually very small, and in many cases it is ignored in controller derivation. Then, the following feedback linearization controller can be defined for the joint torque, extending the controller presented in [17] for a moving base:

$$\tau = g(q_d) + h_D - k_v \tilde{\theta} - d_a \dot{\theta} \tag{19}$$

where $h_D(r_{CoM}, \eta, q^i)$ is a term that compensates the dynamic coupling of the movement of the multirotor base and the other arm. For example, for the *i*-th joint of the first arm, h_D would be the *i*-th row of the coupling terms Ξ_{q1}:

$$\boldsymbol{\Xi_{q1}} = \boldsymbol{M_{rq1}}\ddot{\boldsymbol{r}} + \boldsymbol{M_{\eta q1}}\ddot{\boldsymbol{\eta}} + \boldsymbol{M_{q1q2}}\ddot{\boldsymbol{q}}_{\boldsymbol{2}} + \boldsymbol{C_{q1}}(\boldsymbol{\xi}, \dot{\boldsymbol{\xi}}) \tag{20}$$

Equation (19) also considers a gravity compensation term, $g(q_d)$, whereas $\tilde{\theta} = \theta - \theta_d$ is the position error of the servo. The gravity compensation term $g(\bar{q}(\theta))$ utilizes a collocated variable $\bar{q}(\theta)$ that is statically equivalent to the link side position q, but only depends on θ can be used to improve stability [17][26], although for these arms it has shown little difference and has been omitted since it requires numerical optimization.

The controller in Eq. (19) compensates for the gravity and coupling terms and define an impedance behavior of the link defined by the stiffness coefficient k_v and the damping coefficient d_a. For the compliant joint of the arm of our aerial manipulator, this is equivalent to connecting serially an active elastic element k_a (generated by the software controller), with the physical elastic element k_p that connects the motor output to the link output. The virtual serial stiffness can be computed [26] from:

$$k_v^{-1} = k_a^{-1} + k_p^{-1} \tag{21}$$

An important point here is that, unlike industrial robotic arms which have control frequencies of 1 kHz and larger, the ultra-lightweight arms in the aerial manipulator are severely constrained by the servomotors used, which have a maximum control frequency of around 50 Hz. Thus, the passive response will be instantly but the active response will come at the control frequency of 50 Hz and with some delay. Then, the global compliant behavior of the arm can be seen as an instant response by the elastic element that is "shaped" later to adapt stiffness and damping with the controller.

The main consequence is the different response to different interactions with objects or the environment. For an impact or collision of the arm, the initial response will come only from the passive elements, followed later by the controller action. On the other hand, other interaction tasks as applying forces or grabbing objects with slower variations of the external forces can fully benefit from the physical stiffness or impedance controller combination.

Thus, when designing the compliant arms for safety of the physical interaction of the aerial manipulator, the physical stiffness should be used. One of the main benefits of the mechanical compliance is the ability of the joints to absorb the excess of energy due to motion constraints in grabbing tasks or associated to impacts between the aerial manipulator and the environment. However, the mechanical limit in the deflection of the joints, around 20 – 30 deg in the developed dual arm, involves a limit in the maximum energy that the manipulator can store in a passive way. If it is imposed that $|\Delta\theta_j^i| \leq \Delta\theta_{max}$, then:

$$E_{PC}^{max} = \frac{1}{2}(\Delta\theta_{max})^2 \sum_{i=1}^{2}\sum_{j=1}^{4} k_{p,j}^i \tag{22}$$

where $k_{p,j}^i$ is the joint physical stiffness and E_{PC}^{max} is the maximum passive compliance energy. Denoting by m_T to the total mass of the aerial manipulator, the maximum speed of the platform that can be supported by the arms in a strong impact is:

$$|v_{max}| \leq \sqrt{\frac{2 \cdot E_{PC}^{max}}{m_T}} = |\Delta\theta_{max}| \sqrt{\frac{\sum_{i=1}^{2}\sum_{j=1}^{4} k_{p,j}^i}{m_T}} \tag{23}$$

Taking as reference the values provided in [24] relative to the aerial manipulator weight ($m_T = 6.8\,kg$), the maximum joint deflection ($|\Delta\theta_{max}| = 20\,deg$) and stiffness, it results that $E_{PC}^{max} = 0.89\,J$ and $|v_{max}| = 0.51\,m/s$.

C. Compliant Arm Cartesian Impedance Controller

Most robotic tasks are better defined in Cartesian space and therefore it is convenient to specify the desired stiffness and damping properties of the compliant arm in the Cartesian space. If the Cartesian position error of the TCP is defined as $\tilde{\boldsymbol{x}} = \boldsymbol{x}_d - \boldsymbol{x}$, being $\boldsymbol{x}_d$ the desired position of the TCP, then the controller of the arm joints can be defined as follows:

$$\boldsymbol{\tau} = \boldsymbol{g}(\boldsymbol{q_d}) + \boldsymbol{H_D} - \boldsymbol{J}^{\boldsymbol{T}}(\boldsymbol{K_C}\tilde{\boldsymbol{x}} - \boldsymbol{D_C}\dot{\boldsymbol{x}}) \tag{24}$$

where $\boldsymbol{\tau}$ and $\boldsymbol{g}$ are the vector equivalents of the terms defined in Eq. (19). $\boldsymbol{H_D}$ is the vector dynamic coupling term of the arm. For the first arm, $\boldsymbol{H_D}$ would be the coupling vector $\boldsymbol{\Xi_{q1}}$ given by Eq. (20), expressed in Cartesian coordinates. In Eq. (24), $\boldsymbol{J}$ is the jacobian matrix of the arm and $\boldsymbol{K_C}$ and $\boldsymbol{D_C}$ are diagonal matrices with the corresponding gains for each Cartesian coordinate, which are related to the joint counterpart through Eq. (9). In this case, the Jacobian is computed w.r.t. the position coordinates only, and supposing that the second joint is fixed ($q_2^i = \varphi_i$), as explained in Section III-B.

An important point here is that the Cartesian compliance properties are generated algorithmically by the controller, since the reflected stiffness of the joints at the Cartesian space varies with the position of the arms and the Jacobian, so in practical applications the effective Cartesian stiffness varies slightly when the arms move, as will be seen in Figure 9.

The performance of this virtual variable impedance control scheme is affected by the noise in the discrete-time derivatives involved in Equations (19), (20). Although the deflection $\Delta\theta$ is measured with a potentiometer, a gyroscope was needed for measuring the angular speed of the output link, $\dot{q}$, whereas the servo provides the angular position and differential position, θ and $\dot{\theta}$. The acceleration signal is not necessary if it is imposed that the desired virtual inertia is equal to the physical inertia so the torque error associated to this term is forced to be zero.

V. Experimental Results

The purpose of the experiments is double. First, the model of compliant joint/manipulator described in Sections III-A,B is validated through frequency (V-A) and impact response (V-C), respectively. This analysis is useful for understanding the dynamic behavior of the compliant arms. Second, the force-impedance control capabilities developed in Section IV are demonstrated, using the vision system for this purpose.

A. Frequency Identification of Compliant Joint Actuator

This experiment validates the dynamic compliant model joint described in Section III-A, generating a sine chirp signal in the range 0 – 8 Hz as position reference for the servo. The frequency response, obtained applying the FFT (Fast Fourier Transform) over the servo position and the deflection signal, is represented in Figure 6. As it can be seen, the deflection is almost zero for frequencies below the resonance peak at $f = 2.82$ Hz, when the amplitude of the output link oscillation is maximal, reaching the mechanical limits of the deflection. Note also that the angular position of the servo drops abruptly at this frequency, decreasing from the pole given by Equation (1), whose bandwidth is $f = 1/(2\pi T_{servo}) = 4.5$ Hz.

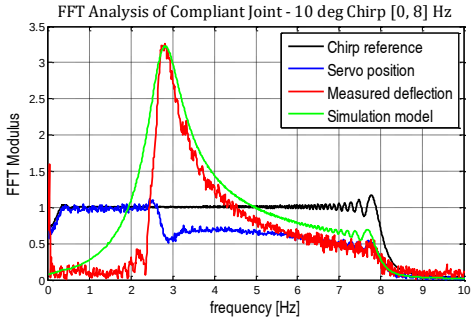

Figure 6. Frequency response of the compliant joint actuator to sine chirp signal generated by the servo. Validation of the mass-spring-damper model.

The value of the damping constant d_p provided in Table 1 was determined matching the simulation model described by Equations (1) – (5) (green line) with the experimental results (red line), known the mass/inertia and stiffness parameters.

B. Virtual Variable Impedance Control: Single Joint Case

The control method given by Equation (19) is evaluated here, comparing the desired simulation response w.r.t. the virtual variable impedance actuator. No torque source is used, instead, the response to the initial condition $q(0) = 90$ deg is considered for simplicity in the realization of the experiments [27]. Figure 7 shows the evolution of the output link position, q, for different values of joint damping, d_v, and stiffness, k_v. The gains of the controller (19) were tuned experimentally for both use cases. Due to model errors and uncertainties, it was found that a small integral term improved the behavior. The control rate was set to 50 Hz, which is in practice the recommended value for preventing packet loss without exceeding the maximum read rate of the servo. A gyroscope attached to the output link was essential for obtaining these results, as it compensates the noise of the deflection signal.

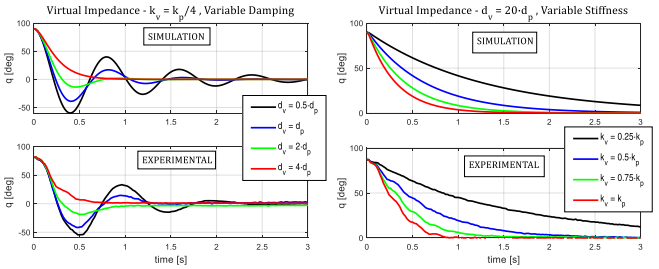

Figure 7. Output link angular position for initial condition $q(0) = 90$ deg: variable damping with $k_v = k_p/4$ (left), and variable stiffness with $d_v = 20 \cdot d_p$ (right). Simulated desired response (up) and experimental (down).

It is necessary to remark that the difference between the simulation and the experimental result may be relatively high due to the unavoidable delay in the actuation. However, the evaluation of the overshoot and the setup time indicates that the virtual impedance is close to the desired one.

C. Impact Response: Cartesian Deflection and Velocity

In aerial manipulation, the transition from contactless to contact situations can be assimilated to an impact between the end effector and the environment. The developed vision system can be exploited for detecting this event, but also for controlling the contact force through the Cartesian deflection of the compliant manipulator. This experiment evaluates the performance of the vision system [28] in dynamic conditions, i.e., measuring the Cartesian deflection and speed when the gripper servo of the left arm is impact by a 62 g weight object thrown from a 0.5 m height (0.3 J energy impact), while the arm rests in L-position (elbow flexion). The position/velocity of the marker is estimated by means of an Extended Kalman Filter (EKF), measuring the acceleration at this point and the joint deflection at 30 Hz. The evolution of these signals can be seen in Figure 8.

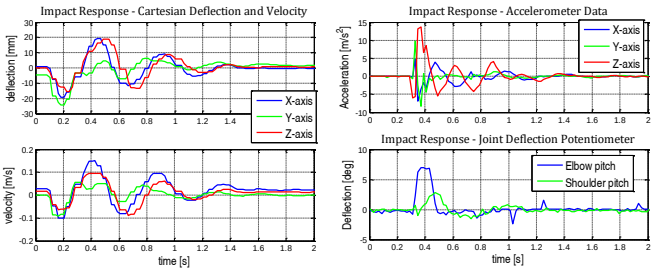

Figure 8. Impact response. Cartesian deflection and velocity measured with the vision system (left). Representation in the frequency domain (right).

The underdamped behavior of the Cartesian deflection to the impulsive response validates the mass-spring-damper model assumed in Equation (8), and also allows the estimation of the Cartesian damping matrix, adjusting its value until the simulation matches the measured response.

D. *Contact Force Control in Hovering Conditions*

The Cartesian compliant controller described in Section IV-C was evaluated in an experiment in which the mobile manipulator approaches to a pipe and exerts a 3 N pushing force with the left arm in the X-axis, maintaining a zero force reference in the YZ axes. The mobile platform approaches to workspace and hovers at a fixed position, while the left arm applies the force on the pipe. The evolution of the experiment can be followed in Figure 9 and Figure 10. The position of the platform is referred to the ARUCO tag placed on the pipe, using two additional markers disposed over the gripper servos for measuring the position of the wrist. As seen on the right side of Figure 9, the joints involved in this task are mainly the shoulder and elbow pitch ones. It is interesting to observe how the Cartesian stiffness slightly varies with the angular position of the joints, as these depend on the Jacobian matrix. The video with the experiments can be seen in [27].

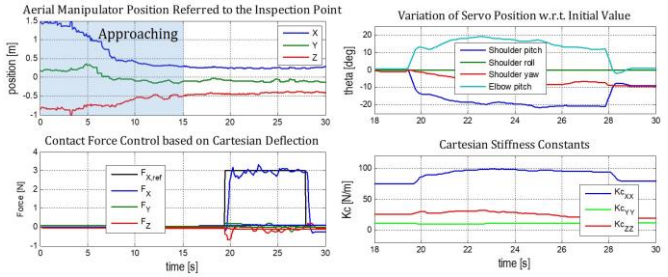

Figure 9. Representative signals in the contact force experiment: position of the platform (up, left), left arm force and reference (down, left), variation of the servos position (up, right), and left arm Cartesian stiffness (down, right).

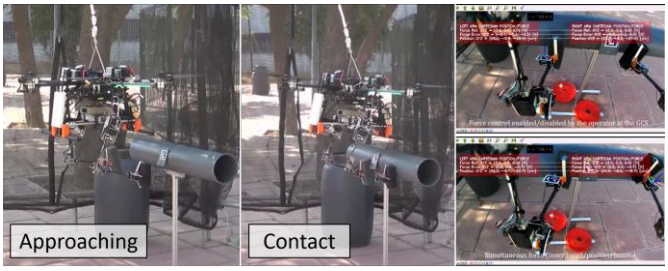

Figure 10. Approaching (left) and contact force control (right) phases seen from the onboard camera. The position of the left/right arms and the target contact point are measured with ARUCO tags.

The structure of the implemented force controller based on Cartesian deflection feedback is represented in Figure 11. This is a variation of the controller given by Equation (24), in which $\boldsymbol{F_e}$ corresponds to the term $\boldsymbol{K_C\tilde{x} - D_C\dot{x}}$, the gravity and the coupling terms $\boldsymbol{g(q_d)}$ and $\boldsymbol{H_D}$ are compensated by the PI force controller block, and the force-torque is obtained from the FK/IK relations instead of using the Jacobian. The position reference of the servos is obtained applying the inverse kinematics over the Cartesian position reference $\boldsymbol{r^i_{ref}}$, which is the sum of the current end effector position and the displacement obtained from a PI force controller, with $K_P = 5\ mm/N$, and $K_I = 5\ mm/Ns$. An initial guess of these values is determined from the maximum Cartesian deflection (~50 mm) and force (~2N) provided by the arms. The control rate was set to 10 Hz, limited mainly by the vision system.

The accuracy in the force estimation was evaluated in test bench using a KERN FKB 8K0.1A bench scale (0.1 grams resolution). Five calibration masses were attached at the tip of the forearm link of the left arm, measuring the Cartesian deflection with the camera head, and estimating their weight from Equation (9). The stiffness of the joints can be found in [24]. Figure 12 shows the payload estimation and the ground truth along with two views of the camera for two masses.

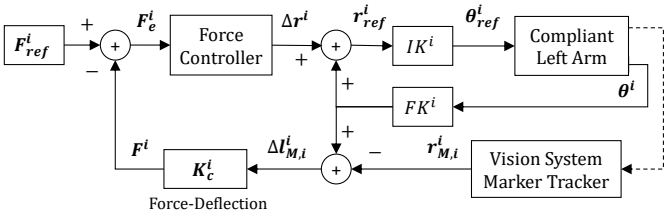

Figure 11. Structure of the force controller based on Cartesian deflection.

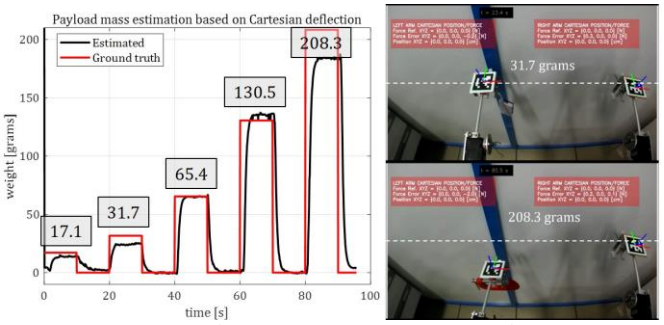

Figure 12. Evaluation of the accuracy in the vision-based force estimation. Different payload masses were attached at the wrist point of the left arm.

E. *Bimanual Object Grasping: Force/Displacement*

During the realization of certain aerial manipulation tasks, it may occur that the robot tries to grasp and retrieve objects whose mass exceeds the payload of the multirotor, or well they cannot be lifted because they are attached to a structure, as the inspection tool shown in Figure 1. One simple way to determine if an object can be retrieved is to apply a pulling force and measure the displacement of the end effector. In Figure 13, a 35 cm length, 0.2 kg weight metal file is grasped with both arms, applying 1 N pulling force (see Figure 11) in the Z-axis in t = 2.3 seconds, which causes a significant displacement of the markers. The experiment is repeated, but now blocking the tool so it cannot be moved. As illustrated in Figure 14, during the 2 s monitoring period, the displacement is below the 1 cm threshold, so then the force ceases and the object is released.

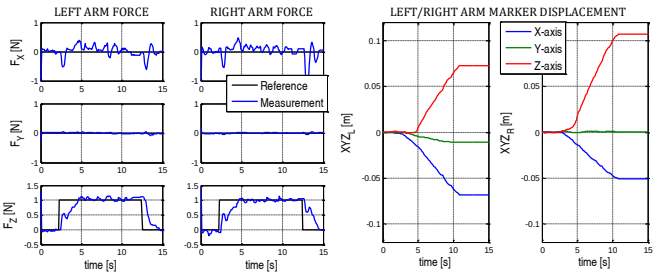

Figure 13. Force (left) and displacement (right) of the left/right arm markers when the grasped object is pulled in the Z-axis and this is lifted.

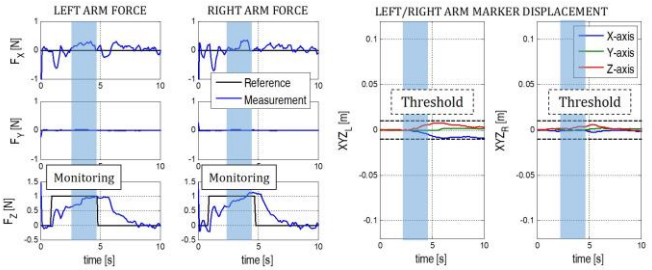

Figure 14. Pulling force and displacement when the object cannot be lifted. The displacement is monitored (blue area) since $F_Z \geq 0.75 \cdot F_{Z,ref}$.

VI. Conclusion

Despite the evident limitations of the smart servo actuators typically employed for building very low weight and low cost aerial manipulators (no torque feedback, only position control with update rates <50-100 Hz), this paper has demonstrated that the force/torque and virtual variable impedance control schemes can be implemented based on the deflection signal of a compliant spring-lever transmission mechanism.

The integration of a vision system in the anthropomorphic, compliant and lightweight dual arm manipulator not only contributes to increase the positioning accuracy, affected by the deflection of the compliant joints, but it also allows to estimate the Cartesian deflection, and thus the force, without the need of additional sensors. As future work, it is proposed the development of an estimator that integrates both vision and joint deflection sensors for improving the accuracy of the force-torque estimation and control.

Acknowledgement

This work has been supported by the AEROARMS project (H2020-2014-644271), funded by the European Commission under the H2020 Programme, and by the AEROCROS (DPI 2015-71524-R) and AEROMAIN (DPI2014-59383-C2-1-R) projects, funded by the Spanish Ministerio de Economia y Competitividad. The research activity of Alejandro Suarez is supported by the Spanish Ministerio de Educación, Cultura y Deporte FPU Program. The authors wish to acknowledge the support provided by Eduardo Suarez in the experiments.

References

[1] Bellicoso, C. D., Buonocore, L. R., Lippiello, V., & Siciliano, B. (2015, June). Design, modeling and control of a 5-DoF light-weight robot arm for aerial manipulation. In 23th Mediterranean Conference on Control and Automation (MED), 2015, pp. 853-858.

[2] Cano, R., Pérez, C., Pruano, F., Ollero, A., & Heredia, G. (2013). Mechanical design of a 6-DOF aerial manipulator for assembling bar structures using UAVs. In 2nd RED-UAS 2013 Workshop on Research, Education and Development of Unmanned Aerial Systems.

[3] Jimenez-Cano, A. E., Martin, J., Heredia, G., Ollero, A., & Cano, R. (2013). Control of an aerial robot with multi-link arm for assembly tasks. In IEEE Int. Conf. on Robotics and Automation (ICRA), 2013, pp. 4916-4921.

[4] Kondak, K., Huber, F., Schwarzbach, M., Laiacker, M., Sommer, D., Bejar, M., & Ollero, A. Aerial manipulation robot composed of an autonomous helicopter and a 7 DoF industrial manipulator. IEEE Int. Conf. on Robotics and Automation (ICRA), 2014, pp. 2107-2112.

[5] Korpela, C., Orsag, M., & Oh, P.. Towards valve turning using a dual-arm aerial manipulator. In IEEE/RSJ Int. Conf. on Intelligent Robots and Systems (IROS), 2014, pp. 3411-3416.

[6] Suarez, A., Jimenez-Cano, A. E., Heredia, G., Vega, V. M., Rodriguez-Castaño, A., and Ollero, A Lightweight and human-size dual arm aerial manipulator. In 2017 Int. Conf. on Unmanned Aircraft Systems (ICUAS), pp. 1778-1784, 2017.

[7] Scholten, J. L., Fumagalli, M., Stramigioli, S., & Carloni, R. Interaction control of an UAV endowed with a manipulator. IEEE Int. Conf. on Robotics and Automation (ICRA), 2013, pp. 4910-4915.

[8] Yüksel, B., Mahboubi, S., Secchi, C., Bülthoff, H. H., & Franchi, A. Design, identification and experimental testing of a light-weight flexible-joint arm for aerial physical interaction. 2015 IEEE Int. Conf. on Robotics and Automation (ICRA), Seattle, WA, 2015, pp. 870-876.

[9] Pounds, P. E., & Dollar, A. M. (2014). Stability of helicopters in compliant contact under PD-PID control. *IEEE Transactions on Robotics*, *30*(6), 1472-1486.

[10] Pratt, J., Krupp, B., & Morse, C. (2002). Series elastic actuators for high fidelity force control. *Industrial Robot: An International Journal*, *29*(3), 234-241.

[11] Yoo, S, and Kyun Chung W. SEA force/torque servo control with model based robust motion control and link-side motion feedback. 2015 IEEE Int. Conf. on Robotics and Automation (ICRA), Seattle, WA, 2015, pp. 1042-1048.

[12] Schiavi, R., Grioli, G., Sen, S., & Bicchi, A. VSA-II: A novel prototype of variable stiffness actuator for safe and performing robots interacting with humans. 2015 IEEE Int. Conf. on Robotics and Automation (ICRA), 2008, pp. 2171-2176.

[13] Fumagalli, M., Barrett, E., Stramigioli, S., & Carloni, R. The mVSA-UT: A miniaturized differential mechanism for a continuous rotational variable stiffness actuator. In *Biomedical Robotics and Biomechatronics (BioRob), 2012 4th IEEE RAS & EMBS International Conference on* (pp. 1943-1948).

[14] Bartelds, T., Capra, A., Hamaza, S., Stramigioli, S., & Fumagalli, M. Compliant aerial manipulators: Toward a new generation of aerial robotic workers. *IEEE Robotics and Automation Letters*, *1*(1), 477-483, 2016.

[15] Mellinger, D., Lindsey, Q., Shomin, M., & Kumar, V. (2011, September). Design, modeling, estimation and control for aerial grasping and manipulation. In IEEE/RSJ Int. Conf. on Intelligent Robots and Systems (IROS), 2011, pp. 2668-2673.

[16] Spong, M. Control of Flexible Joint Robots: A Survey. University of Illinois, Coordinated Science Laboratory Report, 1990.

[17] Ott, C. *Cartesian Impedance Control of Redundant and Flexible-Joint Robots*. Springer, 2008.

[18] Zollo L, Siciliano B, De Luca A, Guglielmelli E, Dario P. Compliance Control for an Anthropomorphic Robot with Elastic Joints: Theory and Experiments. ASME. J. Dyn. Sys., Meas., Control. 2004;127(3):321-328.

[19] V. Lippiello & F. Ruggiero, Exploiting redundancy in Cartesian impedance control of UAVs equipped with a robotic arm, 2012 IEEE/RSJ Int. Conf. on Intelligent Robots and Systems (IROS), Vilamoura, 2012, pp. 3768-3773.

[20] F. Forte, R. Naldi, A. Macchelli & L. Marconi, Impedance control of an aerial manipulator, 2012 American Control Conference (ACC), Montreal, QC, 2012, pp. 3839-3844.

[21] G. Giglio and F. Pierri, "Selective compliance control for an unmanned aerial vehicle with a robotic arm," 22nd Mediterranean Conference on Control and Automation, Palermo, 2014, pp. 1190-1195.

[22] Suarez, A., Heredia, G., & Ollero, A. Lightweight compliant arm for aerial manipulation. In In IEEE/RSJ Int. Conf. on Intelligent Robots and Systems (IROS), 2015 pp. 1627-1632.

[23] Suarez, A., Heredia, G., & Ollero, A. Lightweight compliant arm with compliant finger for aerial manipulation and grasping. In IEEE/RSJ Int. Conf. on Intelligent Robots and Systems (IROS), 2016.

[24] Suarez, A., Ramon-Soria, P., Heredia, G., Arrue, B. C., & Ollero, A. Anthropomorphic, compliant and lightweight dual arm system for aerial manipulation. In In IEEE/RSJ Int. Conf. on Intelligent Robots and Systems (IROS), 2017.

[25] Jimenez-Cano, A. E., J., Heredia, G., & Ollero, A. Aerial manipulator for structure inspection by contact from the underside. In IEEE/RSJ Int. Conf. on Intelligent Robots and Systems (IROS), 2015, pp. 1879-1884.

[26] Petit, F. Analysis and Control of Variable Stiffness Robots. PhD thesis, ETH Zurich, 2014.

[27] https://hdvirtual.us.es/discovirt/index.php/s/39g0bWWhidfDGEy

[28] Suarez, A., Heredia, G., Ollero, A. Vision-based deflection estimation in an anthropomorphic, compliant and lightweight dual arm. In Robot 2017: Third Iberian Robotics Conference, vol. 2, pp. 332-344 (2018).